# Current and field pattern in rectangular and inhomogeneous superconductors

Th. Schuster, H. Kuhn, and E. H. Brandt
*Max-Planck-Institut für Metallforschung, Institut für Physik, Postfach 800665, D-70506 Stuttgart, Germany*

M. V. Indenbom*
*Institut de Génie Atomique, Ecole Polytechnique Fédérale de Lausanne, CH-1015 Lausanne, Switzerland*

M. Kläser and G. Müller-Vogt
*Kristall- und Materiallabor, Universität Karlsruhe, Kaiserstraße 12, 76128 Karlsruhe, Germany*

H.-U. Habermeier
*Max-Planck-Institut für Festkörperforschung, Postfach 800665, 70506 Stuttgart, Germany*

H. Kronmüller and A. Forkl
*Max-Planck-Institut für Metallforschung, Institut für Physik, Postfach 800665, D-70506 Stuttgart, Germany*
(Received 24 May 1995)

The penetration and exit of magnetic flux in type-II superconductors is investigated for the realistic situation where a transverse magnetic field is applied to a square or rectangular plate or film. In rectangular specimens the pattern of the sheet current and of the density of the perpendicular flux has some common features with the one-dimensional distributions in circular disks or long strips. Other features, however, are characteristic for the rectangular shape, e.g., the starlike pattern of the penetrating flux and, in the fully penetrated critical state, the discontinuity lines at which the current stream lines perform sharp bends and at which the perpendicular magnetic field $H_z(x,y)$ exhibits sharp ridges. These typical features have to be calculated from a genuine two-dimensional theory. Such a theory based on a highly nonlinear current-voltage law is outlined. The field patterns obtained by this general theory are compared with patterns observed magneto-optically at the surface of square and rectangular single crystals or films of high-$T_c$ superconductors with homogeneous and inhomogeneous critical-current distribution. It is shown that the analysis of the current-discontinuity lines is essential to understand the flux dynamics in superconductors. In samples with inhomogeneous critical current density $j_c(\mathbf{r})$, a strong concentration of flux motion and electric field can occur along the lines where $j_c$ changes abruptly. This may trigger flux jumps.

## I. INTRODUCTION

The penetration and exit of magnetic flux in realistic type-II superconductors in a time-varying applied magnetic field $H_a$ is a highly nontrivial problem.[1] Recent investigations of the flux distribution in type-II superconductors show a preferential flux penetration along boundaries separating superconducting regions with different critical currents[2,3] or a cushionlike flux penetration into homogeneous polygonal specimens.[2,4–9]. These complicated features can be interpreted by doing experiments on simple and regularly shaped samples and the corresponding model calculations. From a theoretical point of view, the driven motion of flux (when $H_a$ is increased or decreased) or creep of flux (when $H_a$ is kept constant) is a *nonlinear* diffusion problem.[10] The nonlinearity arises from pinning and thermal depinning of the Abrikosov flux lines and may be characterized by a nonlinear current-voltage characteristics, e.g., a power law $E(j) = E_c(j/j_c)^n$ where $E$ is the electric field, $j$ the current density, and $j_c$ the critical current density. One has $n \to \infty$ at zero temperature (Bean model of rigid pinning[11]) $n \gg 1$ in the highly nonlinear regime of flux creep, and $n = 1$ in the ohmic regime, namely, for free flux flow, realized at large current densities $j \gg j_c(T)$, or for thermally assisted flux flow,[12] realized above a depinning temperature, and of course, in the normal conducting state above the transition temperature $T_c$. In general, the flux diffusion coefficient $D$ is related to the resistivity $\rho = E/j$ by $D(j,B,T) = \rho(j,B,T)/\mu_0$.

In addition to being nonlinear, the flux diffusion becomes also *nonlocal* in the realistic experimental situation of thin plates or films in a perpendicular field.[13–16] This nonlocality arises in the limit of thin specimens. In this limit the magnetic field $\mathbf{H}(x,y)$ at the specimen surface and the sheet current $\mathbf{J}(x,y)$ ($\mathbf{j}$ integrated over the specimen thickness) are *two-dimensional* (2D) functions which are related by an integral; this 2D nonlocal relation [Eq. (2) below] follows from the 3D local relation $\mathbf{j} = \nabla \times \mathbf{H}$ (Ampère's law). As a consequence, the 3D diffusion equation $\partial \mathbf{j}/\partial t = D(j,B)\nabla^2 \mathbf{j}$ for the 3D current density $\mathbf{j}(x,y,z,t)$ is replaced by an integral equation for the 2D sheet current $\mathbf{J}(x,y,t)$. The situation becomes more complicated when the finite lower critical field $H_{c1}$

 

and finite reversible magnetization are accounted for;[17] in the present paper the reversible magnetization is disregarded by putting the induction $\mathbf{B} = \mu_0\mathbf{H}$, which is a good approximation for thin high-$T_c$ superconductors.

The present paper focuses on a further realistic complication, namely, on specimens of rectangular shape. In the idealized geometries of a long strip or a circular isotropic disk in perpendicular field, the problem of flux motion becomes *one-dimensional* since the direction of current flow is known and the sheet current $J$ depends only on one spatial coordinate, $\mathbf{J} = \hat{\mathbf{y}}J(x)$ or $\mathbf{J} = \hat{\varphi}J(r)$. For calculations of flux penetration and exit in these simple geometries see Refs. 18–24; magneto-optically measured flux-density profiles nicely agree with these theories even in the case of inhomogeneous superconductors.[25,26] In thin specimens of different shape, however, the flux motion is a genuine 2D problem. Moreover, there appear now *current discontinuity lines* along which the current performs more or less sharp bends and the perpendicular flux density has a pronounced peak.[27] In the limit of a steplike current-voltage law, i.e., in the Bean model with exponent $n \to \infty$, the current streamlines bend sharply and the perpendicular field exhibits a logarithmic infinity along these discontinuity lines. In the ohmic case $n = 1$, discontinuity lines do not occur. In particular, in films or plates of rectangular shape, these discontinuity lines are straight lines starting at the four corners. For an isotropic square the discontinuity lines coincide with the diagonals.

A further difference between disks or infinite strips on one hand, and rectangular plates on the other hand, is that the penetration of flux occurs in a *starlike* pattern, i.e., the flux front is *convex*, penetrating first from the *middle* of the four edges[2,4–9] rather than from the corners. In contrast, the flux front in disks is circular and thus *concave*. As an interesting nontrivial result from our computations we find that the starlike flux front in rectangles appears only if the current-voltage law is nonlinear, e.g., $E \sim j^n$ with $n > 1$; in the ohmic case ($n = 1$) the flux front in rectangles and squares is concave like with the disk. Another important difference between linear and nonlinear current-voltage law occurs for inhomogeneous samples, where for $n \gg 1$ an unusual concentration of flux motion and electric field appears at boundaries separating regions with different $j_c$.

The presented magneto-optical visualization of the flux density at the surface of square or rectangular thin superconductors in combination with the presented theory allows thus to determine homogeneous and inhomogeneous critical current densities and to check various model assumptions and predictions for discontinuity lines and the cushionlike penetration of flux.

The outline of this paper is as follows. In Sec. II the equation of motion for the sheet current in rectangular films is derived and a method for its numerical time integration is outlined. Our magneto-optical method and the sample preparation are described in Sec. III. In Sec. IV our experimental results on square and rectangular high-$T_c$ superconductors with homogeneous and inhomogeneous pinning are presented and compared with theory, and Sec. V summarizes our results.

## II. THEORY

### A. Plates with arbitrary shape

In this section we present a short outline of the general equation of motion for the sheet current $\mathbf{J}(x,y,t) = \mathbf{j}d$ in a thin planar conductor or superconductor of thickness $d$ and arbitrary shape in a time-dependent perpendicular applied field $\hat{\mathbf{z}}\,H_a(t)$. A detailed derivation and further applications to eddy currents, linear ac response, and flux creep are given elsewhere.[28,29] The material will be characterized by $\mathbf{B} = \mu_0\mathbf{H}$ and by a resistivity $\rho = E/j$ or sheet resistivity $\rho_s = E/J = \rho/d$, which may be nonlinear, e.g., a power law $\rho(j) = \rho_c(j/j_c)^{n-1}$ (Ref. 30), or linear, complex, frequency dependent, $\rho = \rho_{ac}(\omega) = \rho' + i\rho''$. In general the nonlinear $\rho$ may depend on $B$ via $j_c(B)$ and $n(B)$, and the linear $\rho$ via the factor $B/B_{c2}$ in the flux-flow resistivity $\rho_{FF} \approx \rho_n B/B_{c2}$, where $\rho_n$ is the normal resistivity. In our theory the sheet resistivity may depend on the position, $\rho_s = \rho_s(x,y)$, either directly in a nonuniform specimen, or indirectly via $J(x,y)$ and $B(x,y)$.

In the present paper we shall apply this general electrodynamic theory to rectangular plates with a static highly nonlinear resistivity, also to inhomogeneous (partly thinned down) plates, and calculate the quasistatic penetration and exit of flux in a slowly cycled applied field.

The equations for the sheet current $J$ and for the perpendicular induction component $B_z = \mu_0 H_z$ in the specimen are obtained as follows. First, one has to express the sheet current by a scalar function $g(x,y)$ as

$$\mathbf{J}(x,y) = -\hat{\mathbf{z}} \times \nabla g(x,y) = \nabla \times \hat{\mathbf{z}}\, g(x,y)\,. \tag{1}$$

This substitution guarantees that $\mathrm{div}\mathbf{J} = 0$ and that the current flows along the specimen boundary if one puts $g(x,y) = \mathrm{const} = 0$ there. In general, the lines $g(x,y) = \mathrm{const}$ coincide with the current stream lines. The physical meaning of $g(x,y)$ is the local magnetization or density of tiny current loops. The integral of $g(x,y)$ over the specimen area yields the total magnetic moment

$$\mathbf{m} = \frac{1}{2}\int \mathbf{r} \times \mathbf{J}(\mathbf{r})\,\mathrm{d}^2r = \hat{\mathbf{z}}\int g(\mathbf{r})\,\mathrm{d}^2r\,. \tag{2}$$

Next one determines the integral kernel $Q(\mathbf{r},\mathbf{r}')$ ($\mathbf{r} = x,y$) which relates the perpendicular field $H_z(x,y)$ in the specimen plane $z = 0$ to the local magnetization $g(x',y')$ by

$$H_z(\mathbf{r}) - H_a = \int_A Q(\mathbf{r},\mathbf{r}')\,g(\mathbf{r}')\,\mathrm{d}^2r'\,, \tag{3}$$

$$g(\mathbf{r}) = \int_A Q^{-1}(\mathbf{r},\mathbf{r}')\,[H_z(\mathbf{r}') - H_a]\,\mathrm{d}^2r'\,, \tag{4}$$

where the integrals are over the specimen area $A$ and $Q^{-1}$ is the inverse kernel, see below. Finding the integral kernel $Q$ is a nontrivial task, since when one performs the limit of zero thickness in the Biot-Savart law, the kernel becomes highly singular, $Q = -1/4\pi|\mathbf{r} - \mathbf{r}'|^3$; this form of the kernel thus applies only when $\mathbf{r}$ lies *outside* the specimen, but *inside* the specimen area (where $\mathbf{r} = \mathbf{r}'$

can occur) one should perform part of the integration analytically to obtain a well behaved kernel.[31] Alternatively, one may obtain this kernel numerically for a small but finite height $z$ above the specimen.[8] Noting that the field of a tiny current loop (or magnetic dipole) of unit strength located at $x = y = z = 0$ with axis along $z$ is

$$H_z(x,y,z) = (1/4\pi)(2z^2 - x^2 - y^2)/(x^2 + y^2 + z^2)^{5/2},$$

one obtains for the kernel

$$Q(\mathbf{r},\mathbf{r}') = \frac{1}{4\pi}\lim_{z\to 0}\frac{2z^2-\rho^2}{(z^2+\rho^2)^{5/2}} \tag{5}$$

with $\rho^2 = (x-x')^2 + (y-y')^2$. The limit $z \to 0$ in (5) can be taken as follows. Noting that

$$\int_\infty \frac{2z^2-\rho^2}{(z^2+\rho^2)^{5/2}}\frac{\mathrm{d}^2r'}{4\pi} = 0$$

is valid for all $z \neq 0$, one may subtract from (3) with (5) inserted this zero-valued integral times $g(\mathbf{r})$. The limit $z \to 0$ can now be taken easily and one gets[31]

$$H_z(\mathbf{r}) - H_a = -\int_A \frac{g(\mathbf{r}')}{4\pi|\mathbf{r}-\mathbf{r}'|^3}\mathrm{d}^2r' \tag{6}$$

for $\mathbf{r}$ outside the specimen area $A$, and

$$H_z(\mathbf{r}) - H_a = C(\mathbf{r})g(\mathbf{r}) - \int_A \frac{g(\mathbf{r}')-g(\mathbf{r})}{4\pi|\mathbf{r}-\mathbf{r}'|^3}\mathrm{d}^2r' \tag{7}$$

for $\mathbf{r}$ inside $A$, with

$$C(\mathbf{r}) = \int_{\infty - A}\frac{\mathrm{d}^2r'}{4\pi|\mathbf{r}-\mathbf{r}'|^3}. \tag{8}$$

The integral (8) is over the infinite area excluding the specimen area. For example, a rectangular plate with $|x| \le a$, $|y| \le b$ has

$$C(\mathbf{r}) = \frac{1}{4\pi}\sum_{p,q=\pm 1}[(a-px)^{-2} + (b-qy)^{-2}]^{-1/2}, \tag{9}$$

which for a long strip with $|x| \le a \ll b \gg |y|$ yields $C(x,y) \approx C(x) = (ab/2\pi)/(a^2-x^2)^{1/2}$. For practical purposes it may seem more convenient to use the integral kernel $Q$ in the original form (5) and choose a small but finite distance $z$ above the specimen plane $z = 0$.[8]

From the integral kernel $Q$ the inverse kernel $Q^{-1}$ may be obtained by Fourier transform (see below) or by introducing a grid with positions $\mathbf{r}_i = (x_i, y_i)$, weights $w_i$, the tables $H_i = H_z(\mathbf{r}_i)$ and $g_i = g(\mathbf{r}_i)$, and the matrix $Q_{ij} = Q(\mathbf{r}_i, \mathbf{r}_j)w_j$. The integrals (3) and (4) then are approximated by the sums $H_i = \sum_j Q_{ij}g_j$ and $g_i = \sum_j Q_{ij}^{-1}H_j$ where $Q_{ij}^{-1}$ is the inverse matrix of $Q_{ij}$.[15,16,8]

As the last step, the equation of motion for $g(x,y,t)$ is obtained from the (3D) induction law $\nabla \times \mathbf{E} = -\dot{\mathbf{B}}$ (the dot denotes $\partial/\partial t$) and from the material laws $\mathbf{B} = \mu_0\mathbf{H}$ and $\mathbf{E} = \rho\mathbf{j}$ valid inside the sample where $\mathbf{j} = \mathbf{J}/d = -\hat{\mathbf{z}} \times (\nabla g)/d$. In order to obtain an equation of motion for $g(x,y,t)$, it is important to note that the required $z$ component

$$\begin{aligned}\dot{B}_z = \hat{\mathbf{z}}\,\dot{\mathbf{B}} &= -\hat{\mathbf{z}}\,(\nabla \times \mathbf{E}) = -(\hat{\mathbf{z}} \times \nabla)\,\mathbf{E} \\ &= -\hat{\mathbf{x}}\,\partial\mathbf{E}/\partial y + \hat{\mathbf{y}}\,\partial\mathbf{E}/\partial x\end{aligned}$$

does not depend on the (unknown) derivative $\partial\mathbf{E}/\partial z$. With the sheet resistivity $\rho_s = \rho/d$ one may write inside the sample $\mathbf{E} = \rho\mathbf{j} = \rho_s\mathbf{J} = -\rho_s\hat{\mathbf{z}} \times \nabla g$ and thus $\dot{B}_z = (\hat{\mathbf{z}} \times \nabla)(\rho_s\hat{\mathbf{z}} \times \nabla g) = \nabla\cdot(\rho_s\,\nabla g)$. Inserting this into Eq. (4) one obtains the equation of motion for $g(x,y,t)$ in the form

$$\dot{g}(\mathbf{r},t) = \int Q^{-1}(\mathbf{r},\mathbf{r}')\,[\,f(\mathbf{r}',t) - \dot{H}_a(t)\,]\,\mathrm{d}^2r', \tag{10}$$

$$f(\mathbf{r},t) = \nabla\cdot(\rho_s\,\nabla g)/\mu_0. \tag{11}$$

This general equation, which applies also when $\rho_s = \rho/d$ depends on $\mathbf{r}$, $\mathbf{J}$, and $H_z$, is easily integrated over time on a personal computer. Since $\rho/\mu_0$ has the meaning of a diffusivity, Eq. (10) describes nonlocal (and in general nonlinear) diffusion of the local magnetization $g(x,y,t)$. When the resistivity is anisotropic Eq. (10) still applies but with modified $f(\mathbf{r},t)$. For example, if $E_x = \rho_{xx}J_x$ and $E_y = \rho_{yy}J_y$, one has

$$f(\mathbf{r},t) = \nabla_x[(\rho_{yy}/d)\nabla_x g] + \nabla_y[(\rho_{xx}/d)\nabla_y g].$$

### B. Rectangular plates

For specimens of rectangular shape the boundary condition that $\mathbf{J}$ flows along the specimen boundary may be satisfied by writing $g(x,y)$ as a 2D Fourier series in which each term vanishes at the edges. For a rectangle filling the area $0 \le x \le 2a$, $0 \le y \le 2b$, this series reads

$$g(x,y,t) = \sum_{\mathbf{K}} g_{\mathbf{K}}(t)\sin K_x x \sin K_y y\,, \tag{12}$$

where the $\mathbf{K}$ are reciprocal-lattice vectors with components

$$K_x = (2m-1)\pi/2a$$

and

$$K_y = (2n-1)\pi/2b, m, n = 1, 2, 3, \ldots;$$

the sum $\sum_{\mathbf{K}}$ is over all $m \ge 1$, $n \ge 1$. For the field $H_z$ *inside* the specimen area one formally may write a similar Fourier series,

$$H_z(x,y,t) = \sum_{\mathbf{K}} H_{\mathbf{K}}(t)\sin K_x x \sin K_y y\,. \tag{13}$$

From (3), (12), and (13) one obtains the relation

$$H_{\mathbf{K}}(t) = \sum_{\mathbf{K}'} Q_{\mathbf{K}\mathbf{K}'}g_{\mathbf{K}'}(t)\,, \tag{14}$$

where the $Q_{\mathbf{K}\mathbf{K}'}$ are the 2D Fourier coefficients of the integral kernel $Q$ in (3),

$$Q(\mathbf{r},\mathbf{r}') = \frac{1}{ab}\sum_{\mathbf{KK}'} Q_{\mathbf{KK}'} \sin K_x x \sin K_y y \times \sin K'_x x' \sin K'_y y' . \quad (15)$$

Explicitly one obtains from (5) and (15)

$$Q_{\mathbf{KK}'} = \frac{2}{\pi^2 ab}\int_0^\infty \mathrm{d}k_x \frac{K_x K'_x(1+\cos 2ak_x)}{(k_x^2-K_x^2)(k_x^2-K_x'^2)} \times \int_0^\infty \mathrm{d}k_y\, k \frac{K_y K'_y(1+\cos 2bk_y)}{(k_y^2-K_y^2)(k_y^2-K_y'^2)} . \quad (16)$$

The integrand in (16) is sharply peaked at $K_x = K'_x$ and $K_y = K'_y$. Without the common factor $k = (k_x^2+k_y^2)^{1/2}$ the double integral (16) would separate and would exactly equal $\frac{1}{2}\delta_{\mathbf{KK}'}$. Therefore, at large $K$ or $K'$ one approximately has $Q_{\mathbf{KK}'} = \delta_{\mathbf{KK}'}K/2$. This highly useful approximation allows to write down the inverse kernel explicitly as $Q^{-1}_{\mathbf{KK}'} = \delta_{\mathbf{KK}'}2/K$ and obtain useful approximate analytic expressions.

### C. Numerical method

The calculation of current and flux distributions in a rectangular film proceeds as follows. One defines an equidistant grid $x_\mu = (\mu - \frac{1}{2})a/N_x$ $(\mu = 1 \ldots N_x)$, $y_\nu = (\nu - \frac{1}{2})b/N_y$ $(\nu = 1 \ldots N_y)$. These $N = N_x \times N_y$ points $\mathbf{r_i} = (x_i, y_i)$ $(i = 1 \cdots N)$ cover one quarter of the rectangle, which suffices because of symmetry.

Then one calculates the $N^2$ Fourier coefficients $Q_{\mathbf{KK}'}$ (16) for $N_x$ values $K_x$ and $N_y$ values $K_y$, i.e. for $m = 1 \ldots N_x$, $n = 1 \ldots N_y$. These $N^2$ double integrals (16) are computed rapidly by two one-dimensional integrations (or matrix multiplications) if appropriate grids for the $k_x$ and $k_y$ are chosen. Note the symmetry $Q_{\mathbf{KK}'} = Q_{\mathbf{K}'\mathbf{K}}$. Next one calculates and tabulates the $N \times N$ symmetric matrix $Q_{ij} = Q(\mathbf{r}_i, \mathbf{r}_j)(ab/N) = Q_{ji}$ from the Fourier series (15). Finally, the inverted matrix $Q^{-1}_{ij}$ is computed and tabulated; this inversion requires $\approx 2 \times N^3$ floating-point operations and takes typically a few seconds to a few minutes on a personal computer if $N_x = N_y = 12$ to 24 is chosen. For a square specimen the additional symmetry reduces the size of the tabulated matrices by a factor of 4. All these computations have to be performed only once for a given side ratio $b/a$ and grid size $N_x \times N_y$.

Using the tabulated matrices $Q_{ij}$ and $Q^{-1}_{ij}$, the equation of motion (10) for the vector $g_i(t) = g(x_i, y_i, t)$ is easily integrated over time, starting with $g_i(0) = 0$. We have done this for various sweep rates $\dot{H}_a(t)$, for cycled $H_a(t)$, and for creep problems $(\dot{H}_a = 0)$, choosing several current-voltage curves or resistivities $\rho(H, J)$. From the resulting $g(x, y, t)$ one obtains the sheet current $\mathbf{J}(x, y, t) = -\hat{\mathbf{z}} \times \nabla g$ and the magnetic field $H_i(t) = H(x_i, y_i, t) = \sum_j Q_{ij} g_j$. Both $J = |\nabla g|$ and $H$ are required at each time step since they enter the resistivity, which was chosen in the form $\rho = \rho(x, y, t) = \rho_0[J/J_c(H)]^{n-1}$, where $J = jd$ and $J_c = j_c d$. Even for large $n = 99$ the numerical method is quite stable when the spatial derivatives in (11) are calculated from Fourier series of the form (12).

A useful check of the accuracy of this numerical method for large exponents $n$ is the vanishing of the magnetic field in a wide region inside the rectangle before flux has penetrated. This is a very sensitive test; the central field vanishes only when the numerical solution yields a shielding current which exactly compensates the applied field in the field-free region. Any flaw or inaccuracy in the numerics would destroy this compensation. Another test of the achieved accuracy is the constancy of the sheet current in the penetrated region when Bean's assumption $J_c(H)$ =const is used. A further useful check of the numerical results is the known analytical solution for a thin rectangular superconductor in the critical state described in the next section.

### D. Critical state in rectangular superconductors

For the particular choices $J_c(H) = \text{const}$ and $n \gg 1$, our computation reproduces the results of the Bean model. In this model the current density in the entire specimen takes its maximum possible value $|\mathbf{j}| = j_c$ if the sample is in the critical state, i.e., fully penetrated by magnetic flux. In addition, the current density has to satisfy the continuity condition $\mathrm{div}\mathbf{j} = 0$ and has to flow parallel to the surfaces. For superconductors with a rectangular cross section it follows from these conditions that the current stream lines have sharp bends; this is a characteristic feature of vector fields with constant modulus.[32] As discussed in the review by Campbell and Evetts,[1] these sharp bends form discontinuity lines ($d$ lines) which divide the superconductor into domains with uniform parallel current flow; see the upper plots in Figs. 1 and 2. One distinguishes two types of $d$ lines:[27] At $d^+$ lines the orientation of $\mathbf{j}_c$ changes discontinuously but the magnitude of $j_c$ remains the same. At $d^-$ lines the magnitude of $j_c$ changes, e.g., at the specimen surface or at inner boundaries where regions of different $j_c$ meet (see Sec. IV C). At such boundaries the current lines have to bend sharply in order to satisfy the condition of continuous current flow. In superconductors which are isotropic in the $x$-$y$ plane, the $d^+$ lines run along the bisection lines starting from the sample corners and on a section of the middle line parallel to the longer side as shown in the middle plots in Figs. 1 for a square and 2 for a rectangle with side ratio $b/a = 1.4$.

Characteristic features of the $d^+$ and $d^-$ lines are the following.

(1) Whereas the $d^-$ lines occur at internal and external boundaries of the sample (local sample geometry), the $d^+$ lines form in homogeneous regions and are determined by the shape of the sample.

(2) Flux lines cannot cross the $d^+$ lines since during increase or decrease of the applied magnetic field the flux motion is directed towards or away from the $d^+$ lines, respectively. In contrast, the $d^-$ lines can be crossed, e.g., when flux lines penetrate from the surface. When the current does not flow parallel to the $d^-$ line, a strong flux motion is directed along the $d^-$ line.

(3) The electric field $E$ is largest at the $d^-$ lines, whereas we have $E = 0$ at the $d^+$ lines. This is discussed

in Sec. IV C.

(4) The $d^+$ and the $d^-$ lines do not change their position during lowering or reversing of the external magnetic field, although the magneto-optically detected intensities of the $d^+$ and $d^-$ lines are reversed in the remanent state. In thin type-II superconductors ($d \ll a$) these $d^+$ and $d^-$ lines are clearly seen because of the logarithmic infinity of $B_z$ at the sample surface.[27]

The rectangular current pattern of the critical state applies to superconductors of arbitrary thickness $d$. The resulting magnetic field, however, depends on $d$. If the specimen cross section is $|x| \leq a$, $|y| \leq b$, then in longitudinal geometry (for large specimen length $d$ along $\mathbf{H_a} \| \hat{\mathbf{z}}$) the magnetic field in the Bean critical state inside the superconductor is

$$H_z(x,y) = H_a - j_c \max(a - |x|,\, b - |y|)\,, \qquad (17)$$

where max(...) denotes the maximum value, and outside the superconductor one has $H_z(x,y) = H_a$. This well-known field profile has constant slopes and looks like a sand pile. In this longitudinal geometry the lines $H_z(x,y) = \text{const}$ coincide with the current stream lines. For intermediate specimen thickness $d$, the magnetic field

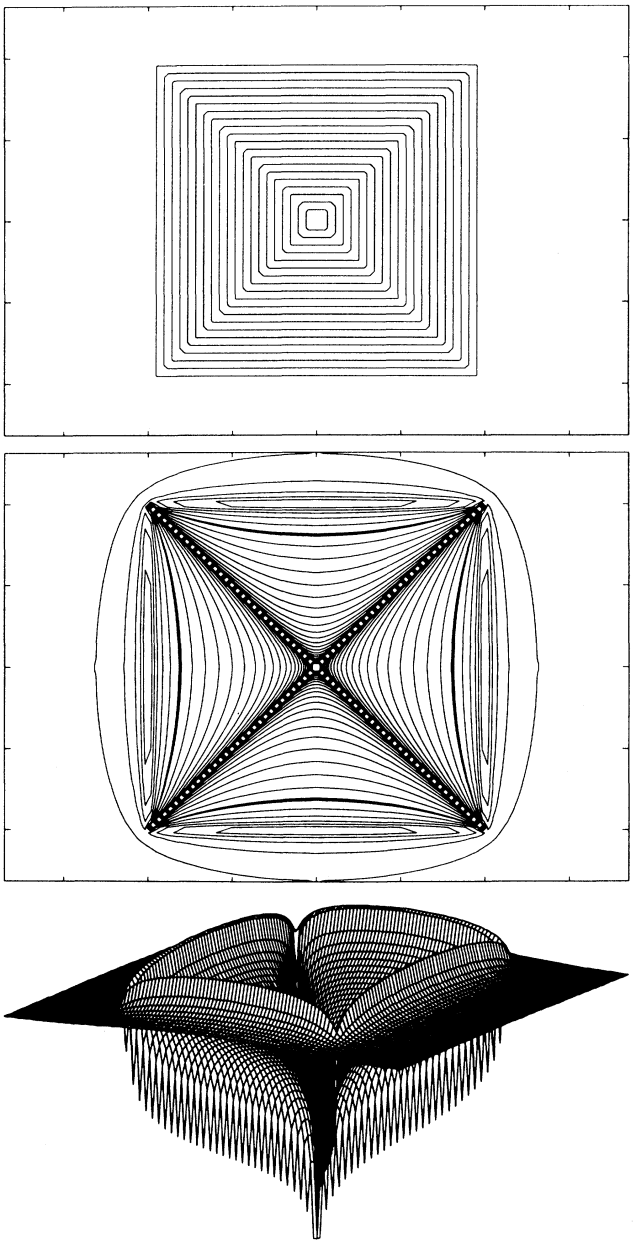

FIG. 1. Top: Stream lines of the current in a thin type-II superconductor of square shape in the critical state. Middle: Normal component of the magnetic field as a contour plot. Bottom: As above but in a three-dimensional plot.

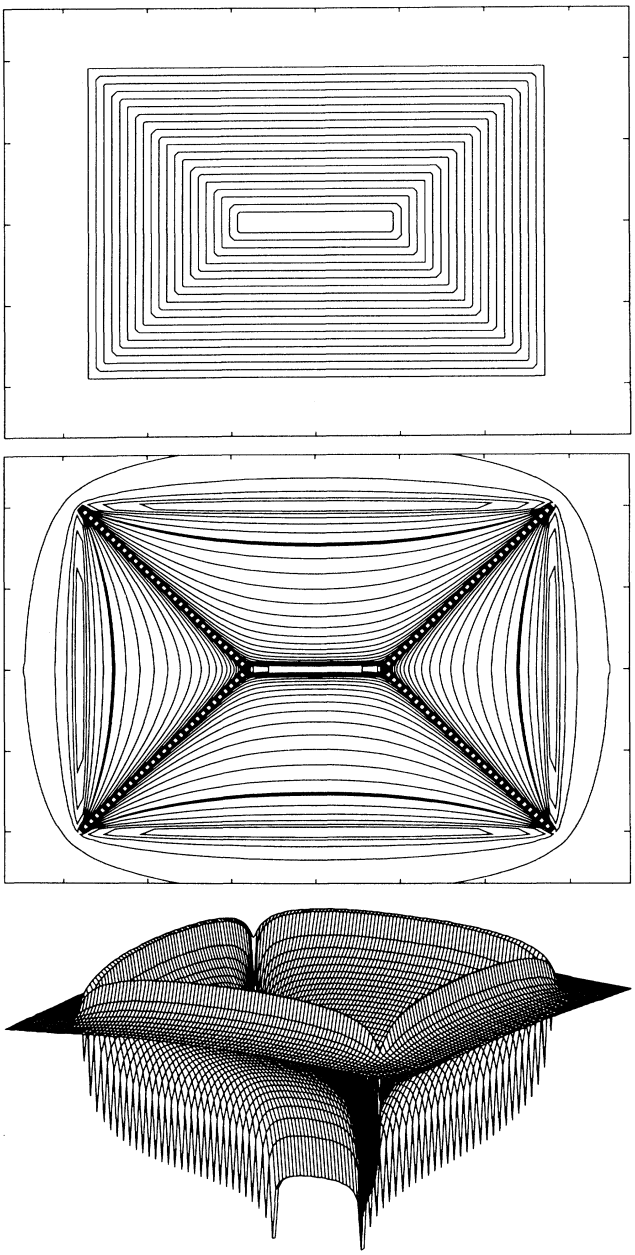

FIG. 2. As in Fig. 1 but for a rectangular shape.

of the rectangular current pattern takes a more complicated form which depends on $d$ in a nontrivial way, see the comprehensive paper by Forkl and Kronmüller.[33] For thin specimens $d \ll a \leq b$, the magnetic field again becomes independent of the thickness. From the Biot-Savart law one finds the following perpendicular field component in the specimen plane $z = 0$ inside and outside the superconductor[34,35]

$$H_z(x,y) = H_a + \frac{J_c}{4\pi} \sum_{p,q=\pm 1} f(px, qy),$$

$$f(x,y) = \sqrt{2} \ln \frac{\sqrt{2}P + a + b - x - y}{\sqrt{2}Q - a + b - x - y} + \ln \left| \frac{(P + y - b)(y - b + a)(P + x - a)\, x}{(y - b)(Q + y - b + a)(x - a)(Q + x)} \right| \tag{18}$$

with $P = [(a-x)^2 + (b-y)^2]^{1/2}$, $Q = [x^2 + (b-a-y)^2]^{1/2}$. This result is different from the field pattern obtained by the sand model[1] which is valid for long samples. In general the sand model gives the local magnetization $g(x,y)$ even for thin specimens. For long samples we have then $g(x,y) \sim H(x,y)$. The field pattern (18) is depicted in Figs. 1 and 2 for the side ratios $b/a = 1$ and $b/a = 1.4$. The "neutral line" $H_z(x,y) = H_a$ is emphasized as a bold line in the contour plots. On this line $H_z$ stays approximately constant during flux creep away from the critical state.[34]

## III. EXPERIMENTS

### A. Faraday effect

We visualize the magnetic field distribution of a superconductor by magneto-optics. Since the high-temperature superconductors (HTSC) themselves have no significant magneto-optical effect, the sample surfaces have to be covered by a magneto-optically active material. For our investigations we use the magneto-optical Faraday effect. The flux penetration is imaged by detecting the rotation of the polarization plane when linearly polarized light passes a magneto-optically active layer exposed to the magnetic field of the underlying superconductor. From flux-free regions the light is reflected without rotation of the polarization plane; this light thus cannot pass an analyzer which is set in a crossed position with respect to the polarizer. In this way the Shubnikov phase (with a flux-line lattice) will be imaged as bright areas, whereas the flux-free Meissner phase remains dark. For the experiments presented in this paper we used ferrimagnetic iron-garnet films with an in-plane anisotropy as magneto-optical indicators.

The iron-garnet film was grown by liquid phase epitaxy onto a gallium-gadolinium substrate with a thickness of about 3.5 $\mu$m (commercial firm Gamma Scientific Production, Russia).[36] This kind of indicator allows the flux penetration into HTSC samples to be observed directly in the whole temperature regime of superconductivity with a magnetic sensitivity of about 1 mT and a spatial resolution of about 4 $\mu$m.

The external magnetic field is generated by a copper solenoid coil, which is cooled with liquid nitrogen and produces a maximum field of 0.55 T. The observations were performed in the optical cryostat described in Refs. 37 and 38. All images can be observed directly via the microscope or be transferred to an image processing system for analyzing.[39] The image processing system allows one to determine the grey level pixel by pixel along a user-defined line.

### B. Sample preparation

The $YBa_2Cu_3O_{7-\delta}$ (YBCO) single crystals were prepared at the Universität Karlsruhe by the self-flux method described in Ref. 40. All crystals have a distinct twin structure which was revealed by polarized light microscopy. The $c$-axis-oriented YBCO thin films were produced at the Max-Planck-Institut für Festkörperforschung in Stuttgart, Germany, by a laser-ablation technique.[41] The thin films were patterned chemically to squares with a lateral length of 1.5 mm. The experiments on superconductors with inhomogeneous pinning were performed on partly thinned down YBCO single crystals.

## IV. RESULTS AND DISCUSSION

### A. Square

To point out the excellent qualitative agreement between theory and experiment we compare calculated distributions of the normal field component $H_z$ with magneto-optically determined flux patterns for rectangular samples. First we show that our theory holds not only for flux penetration but also for flux exit and reverse of the external magnetic field.

In Fig. 3 the left column shows the calculated current pattern in a *square* for different flux-penetration depths. The density of the stream lines gives the magnitude of the current density. In the middle column the contour plots of the corresponding field distributions are plotted. The right column shows magneto-optically detected flux distributions in a thin YBCO film for the three different perpendicular external magnetic fields $\mu_0 H_a = 54$ mT (top row), 92 mT (middle row), and 151 mT (bottom row); the same $H_a$ values were used in the theory. The experiments were carried out at $T = 50$ K using a ferrimagnetic iron-garnet indicator. The white areas correspond to the Shubnikov Phase, into which the flux lines have already penetrated, whereas the flux-free Meissner phase remains dark. The field distributions in the middle column were calculated only inside the sample.

In our transversal geometry the shielding currents flow in the *whole* sample to ensure $B_z = 0$ in the Meissner area, in contrast to the longitudinal geometry, where the shielding currents flow only in the penetrated regions. Comparing the three current distributions one finds that during magnetization the shielding currents change their

magnitude and their direction until the critical value $j_c$ is reached. At places where the shielding current has reached $j_c$ the current flow stays parallel to the sample edges. The current streamlines turn monotonically from the initial concave shape during full screening parallel to the edges. During virgin flux penetration the streamlines never become convex as was supposed in Ref. 6. We find that the regions with $j = j_c$ grow from the middle of

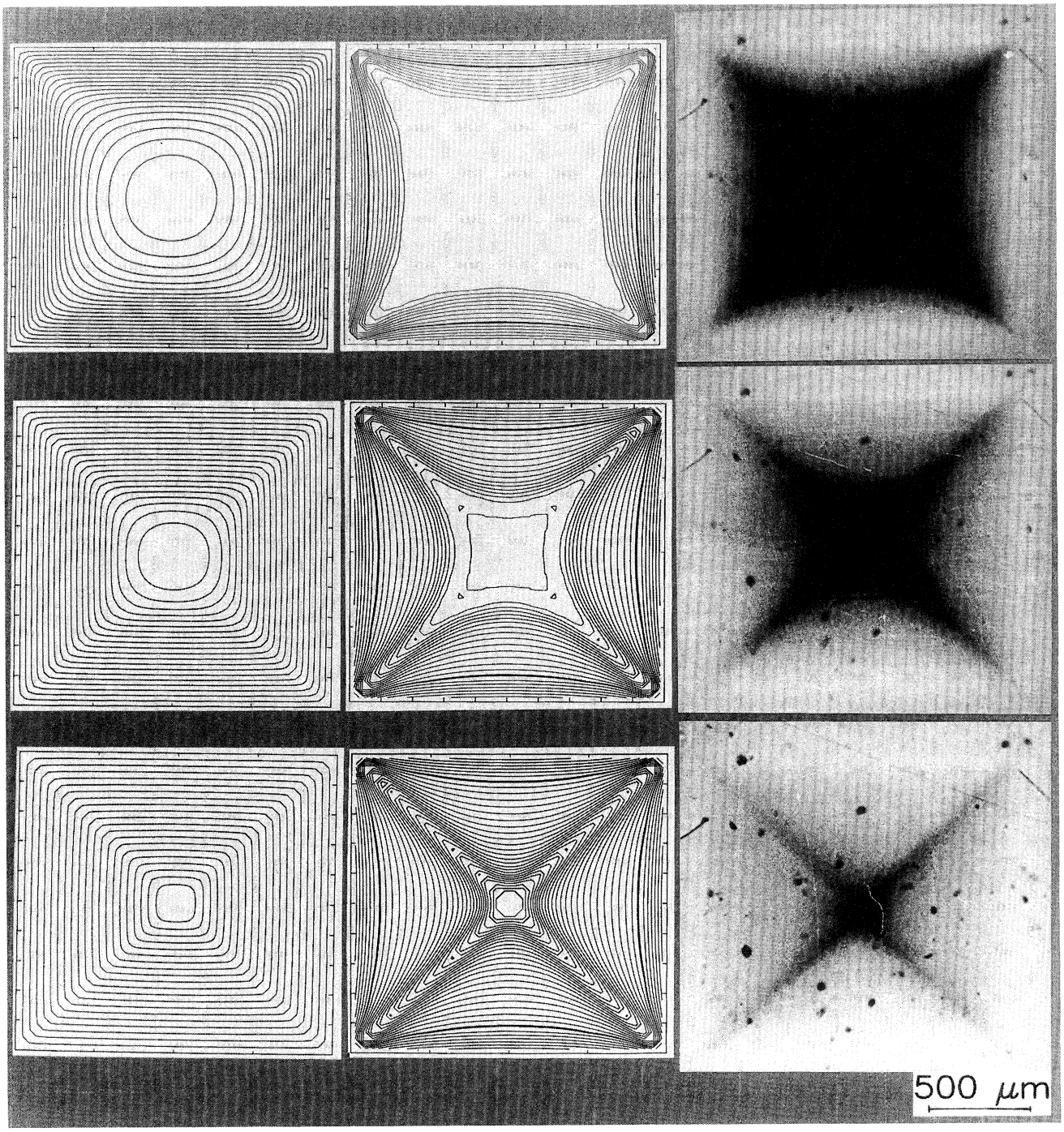


FIG. 3. Calculated current pattern (left column) and perpendicular field $H_z$ (middle column) distribution of a square sample for three different steps of flux penetration. Right column: Magneto-optically detected flux distributions in a square YBCO thin film at $T = 50$ K and $\mu_0 H_a = 54$ mT (top), 92 mT (middle), and 151 mT (bottom). The flux distributions were detected using a ferrimagnetic iron-garnet indicator. The black spots are defects in the indicator film. The film thickness is $d = 800$ nm. In the calculations the unit of the magnetic field (one fit parameter) is chosen such that best agreement is found with the observed flux distributions.

the sample edges. The current-generated magnetic field, which is oriented with the external magnetic field outside the sample, superimposes to the external magnetic field such that a large field enhancement is observed at the sample edges. This overshoot is maximum in the middle of the sample edges. As a result, the magnetic flux penetrates the samples in a cushionlike pattern, i.e., from the middle of the edges rather than from the sample corners as could be expected naively. The neutral line, where the flux profile intersects the value of the external field, is emphasized as a bold line in the contour plots of the magnetic-field distribution. The flux-free white zone in the sample center is the Meissner phase. The numerically calculated flux distributions agree not only with the magneto-optical images in the right column in Fig. 3 but the critical state also coincides with the analytical solution shown in Fig. 1. The above-referenced $d^+$ lines are visible in the magneto-optical images of the critical state as dark lines running along the diagonals.

In decreasing external field the flux lines exit the sample due to the reversal of the driving Lorentz force. This is shown in Fig. 3 for $\mu_0 H_a = 88$, 30, and 0 mT (remanent state). The reversal is caused by the flip of the current from $+j_c$ to $-j_c$, which occurs near the sample edges. As soon as the direction of the change of $H_a$ is reversed, the current density falls below $j_c$ everywhere; relaxation will therefore stop effectively.[22] The turn of the current direction is seen from the loops in the current pattern in the left column in Fig. 4. At the zero line of the current the current-generated magnetic fields of both domains of opposite current direction are oriented parallel to each other. This leads to a maximum in the magnetic-field distribution there; see the loops in the contour plots of the magnetic-field distribution depicted in the middle column and the magneto-optical images in the right column in Fig. 4. The exiting flux lines cause a dark zone of reduced flux-line density which spreads from the edges into the sample. On reaching the remanent state ($H_a = 0$, bottom row in Fig. 4) flux lines with opposite sign, as compared to the pinned ones, start to penetrate the sample and partly annihilate with the pinned flux lines.[42] The boundary between regions containing flux lines of opposite polarity is indicated by the bold line $H_a = 0$ in the middle plot in the bottom row in Fig. 4. In the remanent state the $d^+$ lines are visible as bright lines since the logarithmic infinity of $H_z$ there changes its sign during field decrease. In the magneto-optical image in the bottom row in Fig. 4 $d^+$ lines in the sample center are however dark because the critical state was not yet reached in the maximum applied field; see bottom row in Fig. 3.

When the external magnetic field is decreased further the front of the flux lines with opposite sign and the domain of reversed current flow are shifted towards the sample center. This situation is depicted in Fig. 5 for $\mu_0 H_a = -24$ mT (top), $-42$ mT (middle), and $-80$ mT (bottom row).

The good agreement of the experimental and theoretical pictures demonstrates the validity of our electrodynamical description of a thin square superconductor in a transverse magnetic field during the whole magnetization loop. In the following we present results for rectangular and inhomogeneous samples during flux penetration. The behavior during flux exit is not shown but exhibits equally good agreement.

### B. Rectangle

As can be seen from Fig. 6 the results obtained for a rectangular sample are similar to the ones of the square. The main difference is the occurrence in the critical state of a central $d^+$ line running in the middle of the sample parallel to its longer sides (right column). This $d^+$ line is caused by the collapse of the central current loop to a straight line where two regions of opposing currents meet.

From Fig. 6 one can see that the flux begins to penetrate into the isotropic sample faster from the long than from the short edges. Note that this flux distribution is not caused by an anisotropic current distribution. The ratio between the flux penetration depths in the middle of the short and long edges changes from 0.85 (left column) to 0.92 (middle column) to 1 in the critical state (right column). Naively one might expect faster flux penetration from the short edges because the magnetic-field lines have to make a bigger detour there and thus exert a higher pressure on the short edges. But in reality the field lines take the shorter path and preferentially flow around the middle of the longer edges. Furthermore we observe that the flux front moves towards the loci where the $d^+$ lines will appear and the vortex motion has come to a halt because these important lines cannot be crossed. From this observation the convex shape of the flux front follows naturally.

### C. Inhomogeneous critical-current distribution

In this section we show that our theoretical description also works for samples with an inhomogeneous critical-current distribution. For the experiments we used a rectangular YBCO single crystal with side ratio $b/a = 3$ and thickness $d = 40$ $\mu$m. The sample was partitioned into three equal parts with square shape. In order to induce an inhomogeneity in the critical sheet current we thinned down both outer parts to about $(2/3)d$. For the calculation of the current and field distribution we used the same geometry and a ratio of the critical sheet currents in the central and outer parts $J_c^c/J_c^o = 1.5$. Figure 7 shows the calculated current and flux patterns and experimentally determined flux distributions for this crystal at $T = 20$ K for three different magnetic fields of $\mu_0 H_a = 128$ , 213, and 299 mT (from top to bottom). The experimental images were obtained by magneto-optics using a ferrimagnetic iron-garnet indicator. The black spots on the images are defects in the indicator film. For each magneto-optic image (right column) the corresponding calculated current pattern is depicted above the contour plot of the theoretical flux distribution (left column). The contour $B_z = \mu_0 H_a$ is emphasized as a bold line. The different sheet currents are indicated by different streamline den-

sities. In the region with $J_c^c$ the central streamline loops do not intersect the boundary, at which $J_c$ jumps.

Since the streamlines bend not only at the sample corners but also in the central area near the jump of $J_c$, we observe a complicated $d$-line structure in the critical state (bottom row in Fig. 7). In addition to the $d^-$ lines at the sample edges we have a $d^-$ line running along the boundaries at which the sheet current changes from $J_c^c$ to $J_c^o$. In the central region additional $d^+$ lines run along the lines which connect the bending points of the streamlines. The other $d^+$ lines within the sample are due to the rectangular geometry of the *whole* crystal. For clarity, the $d$-line structure is drawn in one half of the sample in the bottom row in Fig. 7. The central $d^+$ lines in the thinned-

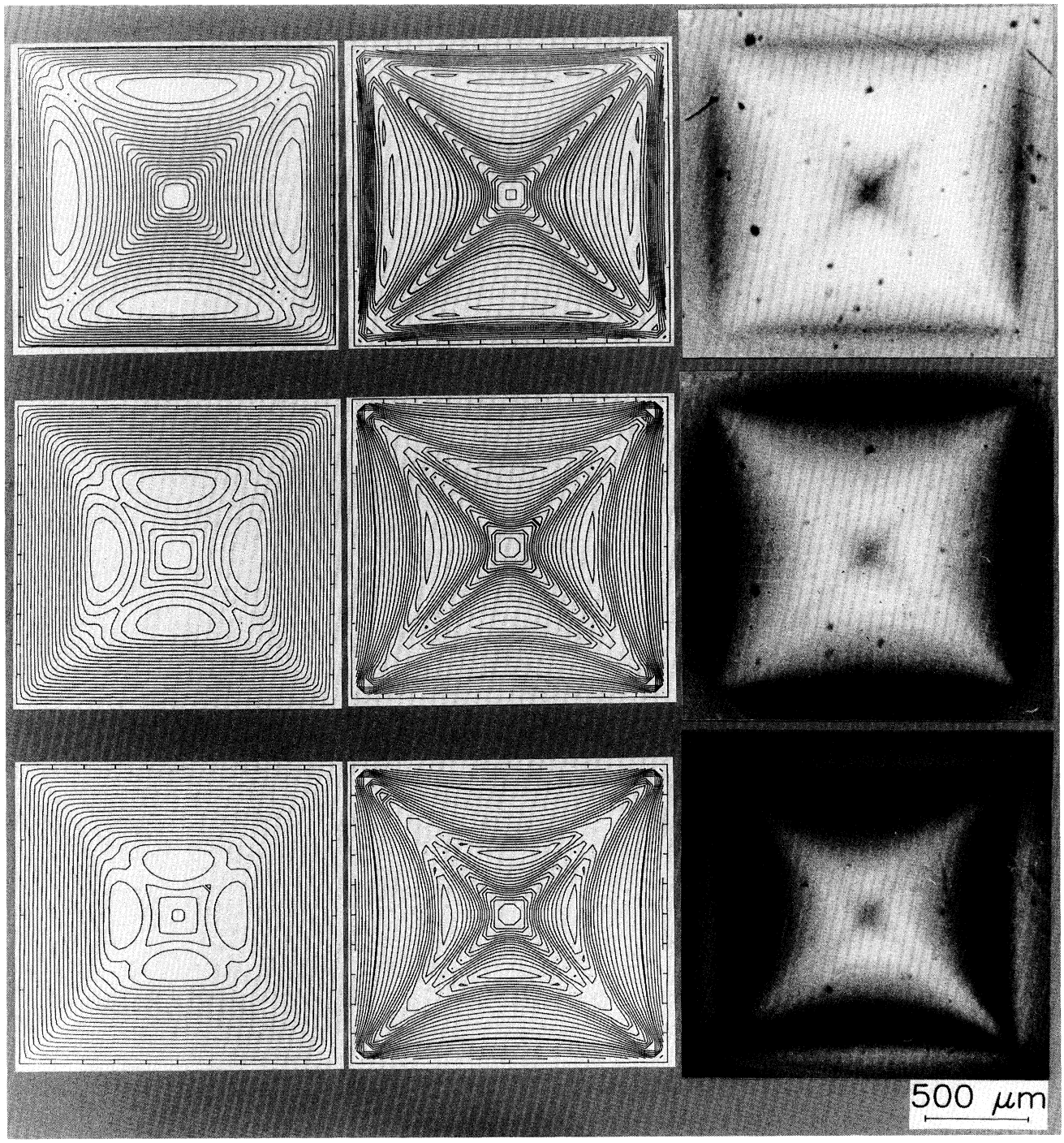


FIG. 4. As Fig. 3 but in decreasing magnetic field. Top: $\mu_0 H_a$ = 88 mT, middle: 30 mT, bottom: 0 mT (remanent state).

down sample regions are hardly visible in the magneto-optical image in the bottom row in Fig. 7, since $H_a$ is increased above the full penetration field of these areas $H^{*o} \approx (J_c^o/2)\ln(4a/d)$ to $H^{*c} \approx (J_c^c/2)\ln(4a/d)$. The calculated flux patterns nicely agree with the magneto-optically determined flux distributions.

In the critical state the ratio $J_c^c/J_c^o$ can be determined from the angle $\alpha$ between the $d^-$ line along the boundary and the $d^+$ line running into the central region, see Fig. 8, via $J_c^c/J_c^o = 1/\cos 2\alpha = 1.5$ (Ref. 27).

If we determine the ratio $J_c^c/J_c^o$ from the different flux penetration depths[21,22] on both sides of the boundaries separating regions with different $J_c$, we obtain a value of about 2, which is larger than the thickness ratio of 1.5. This apparent contradiction can be resolved by considering the current flow through such a boundary: The larger

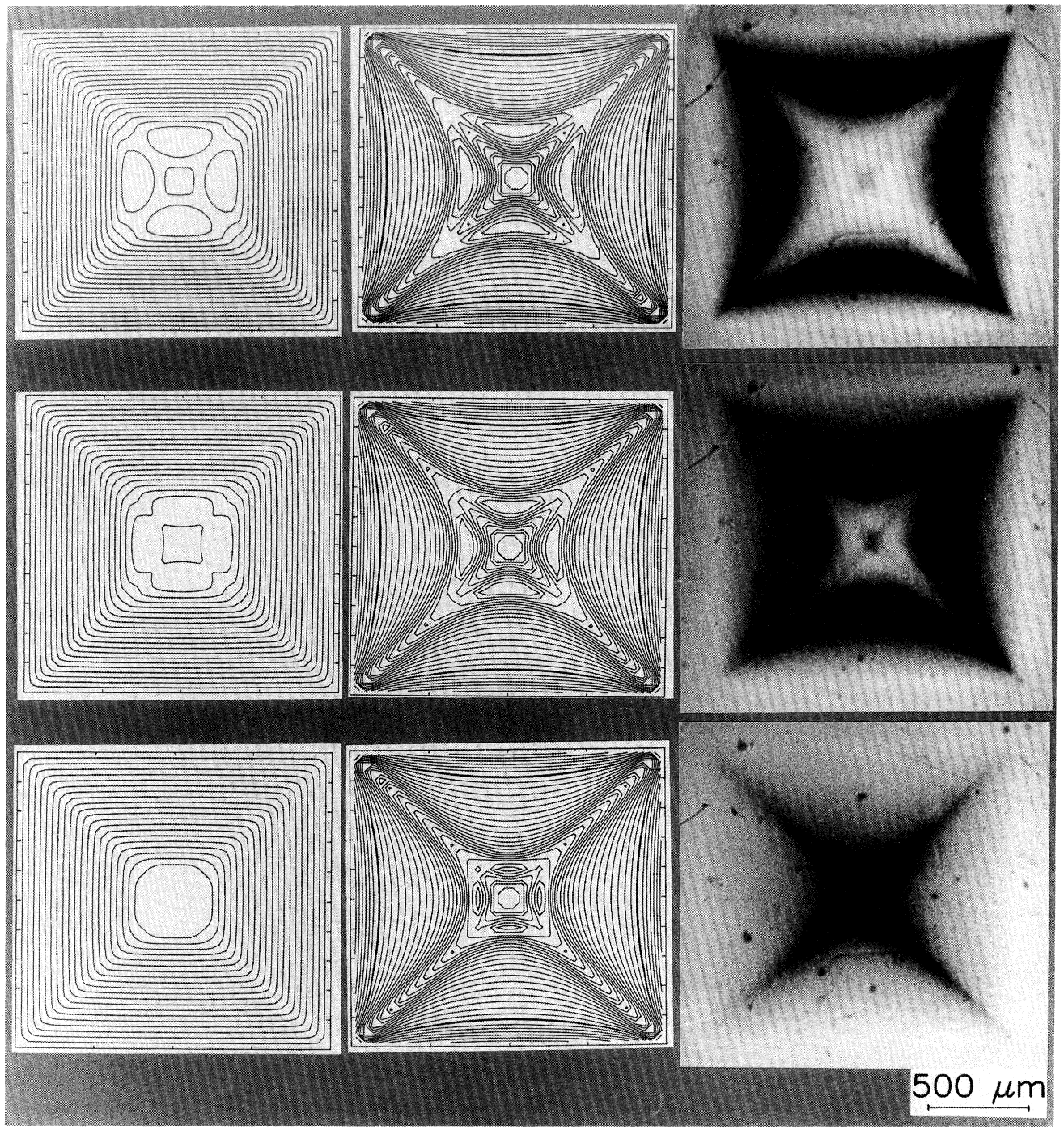


FIG. 5. As Fig. 3 but in reverse magnetic field. Top: $\mu_0 H_a = -24$ mT, middle: $-42$ mT, bottom: $-80$ mT.

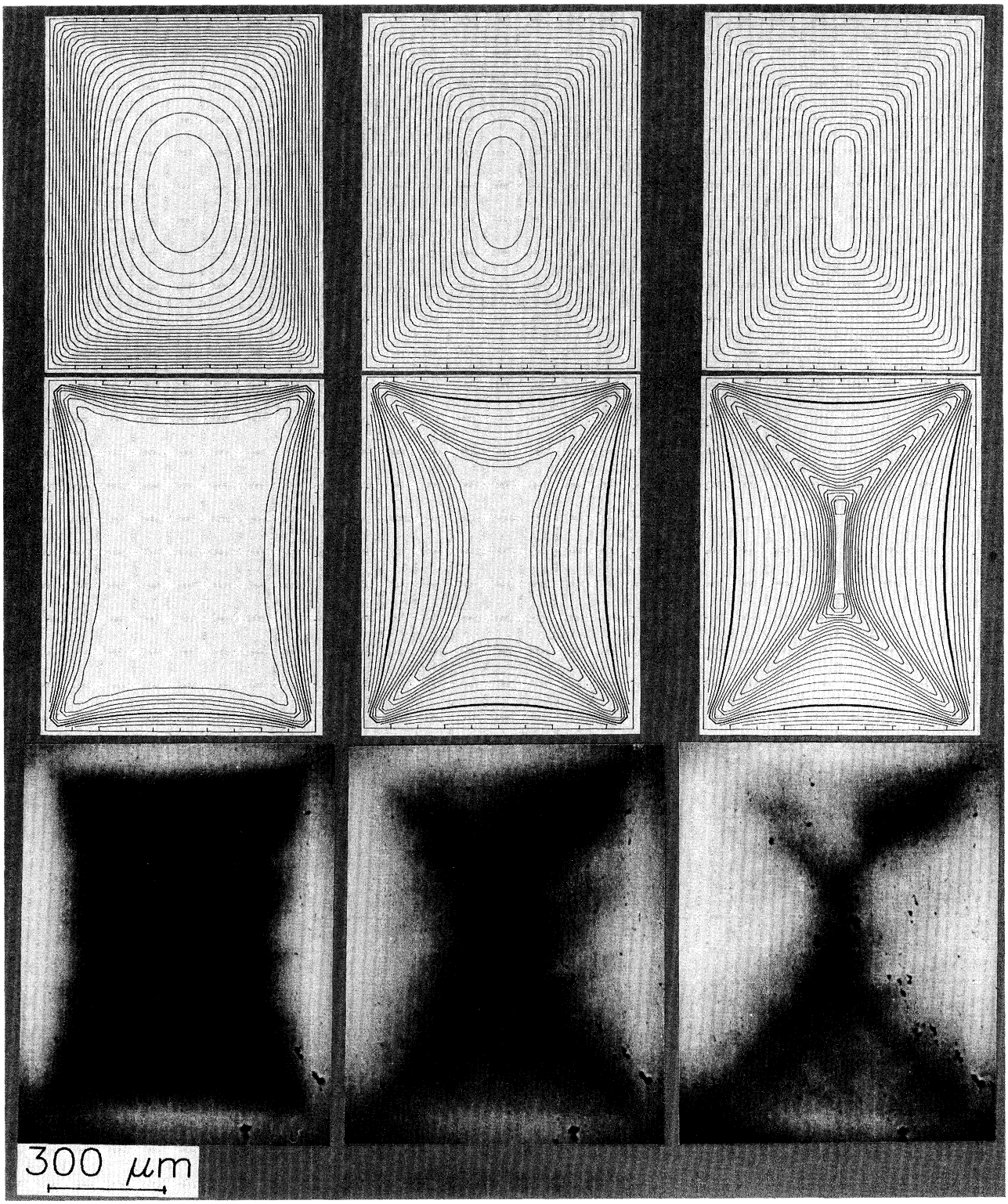


FIG. 6. Calculated current pattern (top) and field $H_z$ (middle row) in a rectangular sample for three different steps of flux penetration. Bottom: Magneto-optically detected flux distributions in a rectangular YBCO single crystal at $T = 30$ K and $\mu_0 H_a = 85$ mT (left), 171 mT (middle column), and 256 mT (right). The flux distributions were visualized using a ferrimagnetic iron-garnet indicator. The black spots are defects in the indicator film. The crystal thickness is $d = 20$ $\mu$m.

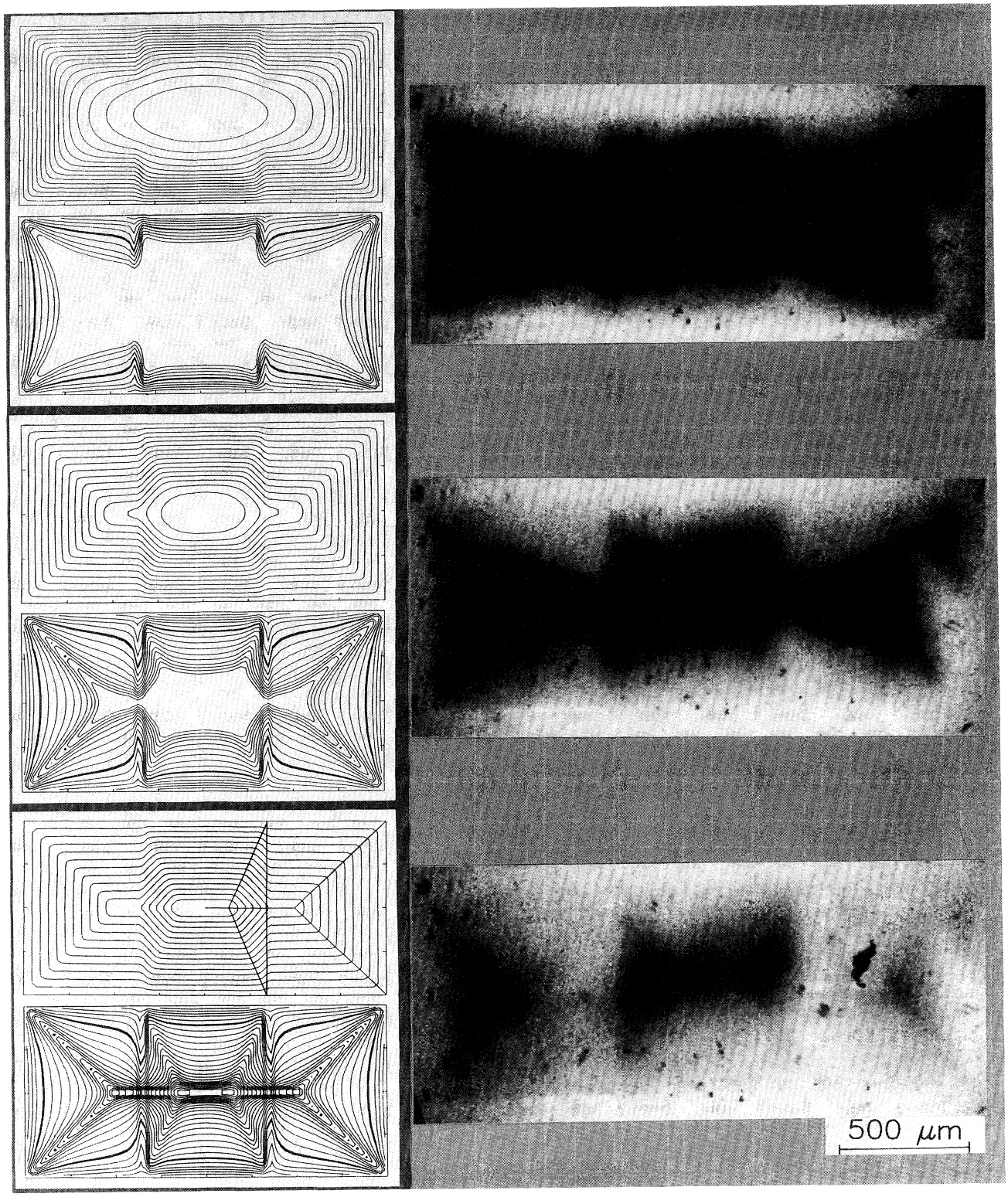


FIG. 7. Calculated current and flux patterns and magneto-optically determined flux distributions in a rectangular YBCO single crystal with inhomogeneous critical current distribution for three different magnetic fields of $\mu_0 H_a = 128$, 213, and 299 mT (from top to bottom). The critical sheet current in the left and right part is about a factor 2/3 lower than the critical sheet current in the central region. For each magneto-optic image (right column) the calculated current distribution is located above the contour plot of the flux pattern (left column). Note the agreement between theory and experiment.

sheet current $J_c^c$ coming from the central part bends in order to satisfy the continuity equation div $\mathbf{J} = 0$, such that the normal component of $\mathbf{J}$ through the boundary equals the lower sheet current $J_c^o$. The resulting jump of the tangential component of $\mathbf{J}$ along the boundary then produces a sharp *positive* ridge of the magnetic field $H_z$ on top of the smooth field which is generated by the entire current distribution and by the external coil. By the same token a *depression* of $H_z$ occurs at the two $d^+$ lines adjacent to this boundary. Combined, these three negative-positive-negative ridges of $H_z$ mean a *concentration* of flux which is seen in Fig. 7 as a deeper flux penetration along the boundary, particularly into the region of lower $J_c$.

Another interesting effect which can be concluded directly from the $d$-line structure in the fully penetrated critical state, concerns the *velocity* of the penetrating flux, which diverges along the boundary where $J_c$ changes abruptly. The region around the boundary where $J_c$ jumps is depicted enlarged in Fig. 8, in which we have chosen a ratio of 2 between the sheet currents (1.5 in Fig. 7) in order to get a larger angle $\alpha = 30°$ for clarity. The streamlines are drawn as bold lines. Our area of interest is the *enclosed triangular region* where the current does not flow parallel to the sample edge. This triangle is bounded by $d^+$ lines at the sample center (top) and at the right (solid line) and by the $d^-$ line running along the boundary at the left. The flux lines move perpendicular to the current flow towards the $d^+$ lines but do not cross these lines as indicated by the dashed arrows. This means that the flux lines can penetrate into the triangular region *only along the boundary* and from there along lines perpendicular to the current streamlines towards the right and upper $d^+$ lines. The density of the dashed lines along the boundary is proportional to the velocity of magnetic flux $|Bv|$ or to the induced electric field $E$. The velocity of the magnetic flux (the height of the ridge of $E$) at a given point on this boundary is proportional to that partial area of the triangle which is filled by the flux passing through this point.[27] For example, all flux lines which flow into this triangle have to pass through the point where the boundary hits the specimen edge, but less flux lines pass through the inner points of the boundary and no flux passes through the midpoint. As a consequence, $E$ varies along this boundary like an $S$ shape, composed of two parabola, beginning and ending with slope zero; see the right plot in Fig. 8.

A 3D plot of the electric-field distribution $E = |\mathbf{E}|$ calculated by the method of Sec. II (see also Refs. 28, 29) is depicted in Fig. 9 for the critical state of our sample in further increasing $H_a$. The ridge of $E$ along the boundary nicely agrees with the $S$ shape depicted in Fig. 8. We find that $E$ is maximum at the $d^-$ lines, while at the $d^+$ lines we have $E = 0$. This is in agreement with the statement that flux lines can cross only the $d^-$ lines but not the $d^+$ lines. Note that the high and narrow ridges of the electric field or of flux flow at internal boundaries where $J_c$ changes abruptly cause enhanced dissipation which may trigger flux jumps.

## V. CONCLUSION

In this paper we have investigated by theory and experiment the penetration and exit of magnetic flux, and the circulating sheet current induced by a cycled applied field $H_a$, in superconducting flat rectangles with uniform or nonuniform pinning. Our theoretical description of flux motion in perpendicular geometry is based on classical electrodynamics in the planar approximation, assuming $H_{c1} = 0$. The magneto-optically observed cushionlike flux penetration in rectangular samples is repro-

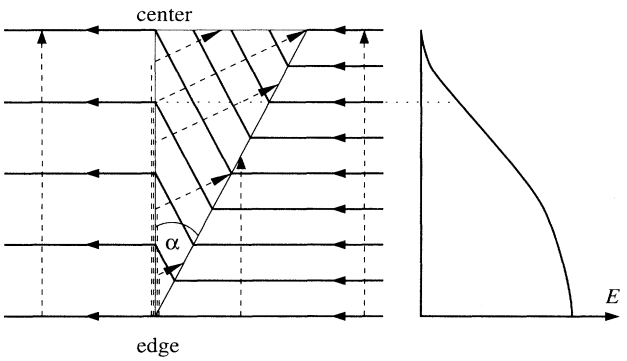


FIG. 8. Visualization of the enhanced flux flow or electric field along the boundary where the critical current density $j_c$ or the critical sheet current $J_c$ abruptly change; cf. also Figs. 7 and 9. The bold lines denote the current flow and the dashed lines the flow of the magnetic flux in form of flux lines. The $S$-shaped flow density profile is depicted in the plot to the right and coincides with the high narrow ridge of $E$ in Fig. 9. The point of inflection in the flow-density profile is marked by a dotted line.

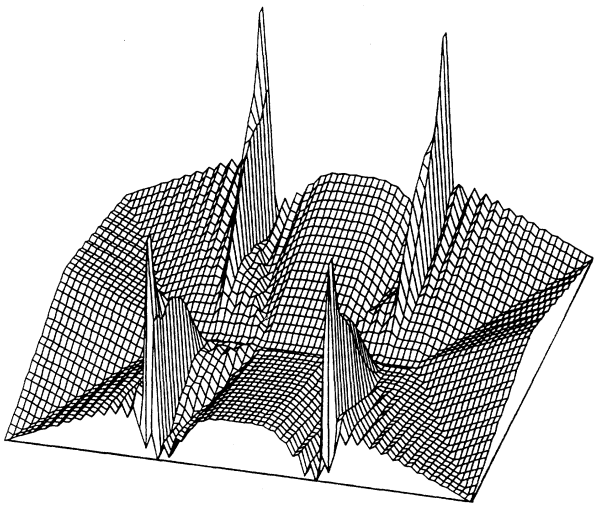

FIG. 9. 3D plot of the electric-field distribution of the inhomogeneous sample shown in Fig. 7 when $H_a$ is increased further after full penetration. The straight lines along the sample edges mark $E = 0$. The physical meaning of the depicted quantity is the velocity of magnetic flux $|Bv|$.

duced only if a nonlinear current-voltage law is assumed. In contrast to surface shielding currents in longitudinal geometry, the shielding currents in flat samples flow immediately across the entire superconductor when a transverse magnetic field is applied. In rectangular samples the streamlines of the shielding currents are always concave for $j < j_c$ and parallel to the edges in the penetrated regions with $j = j_c$. In ohmic rectangles the streamlines are all convex.

We observe that in rectangles the flux begins to penetrate from the long edges faster than from the short edges. This finding is attributed to the partly expelled magnetic-field lines, which concentrate in the middle of the long edges and avoid the short edges.

In inhomogeneous samples the unexpected flux penetration at the boundary separating regions with different critical currents is well reproduced by our model. The deeper flux penetration along this boundary can be explained by ridges of the magnetic field induced by the discontinuity of the tangential component of the current at the boundary, or by the concentration of the electric field along the boundary. An electric-field concentration means a high flux-flow rate and dissipation of energy. This can trigger thermal flux jumps, which should be avoided in high-current applications of superconductors. In all considered cases we found qualitative agreement between our theoretical and experimental flux-density profiles.

## ACKNOWLEDGMENTS

Part of this work was financially supported by the Bundesministerium für Bildung, Wissenschaft, Forschung und Technologie (Grant No. 13N6510). This is gratefully acknowledged. One of us (M.V.I.) is grateful to Fond National Suisse de la Recherche Scientifique (FNPN30 Grant No. 4030-32794).

* Permanent address: Institute of Solid State Physics, Russian Academy of Sciences, Chernogolovka, 142432 Moscow, Russian Federation.

[1] A. M. Campbell and J. E. Evetts, *Critical Currents in Superconductors* (Taylor & Francis, London, 1972).
[2] Th. Schuster, M. Leghissa, M. R. Koblischka, H. Kuhn, H. Kronmüller, and G. Saemann-Ischenko, Physica (Amsterdam) C **203**, 203 (1992).
[3] Th. Schuster, H. Kuhn, M. R. Koblischka, H. Theuss, H. Kronmüller, M. Leghissa, M. Kraus, and G. Saemann-Ischenko, Phys. Rev. B **47**, 373 (1993).
[4] R. P. Huebener, V. A. Rowe, and R. T. Kampwirth, J. Appl. Phys. **41**, 2963 (1970).
[5] V. K. Vlasko-Vlasov, M. V. Indenbom, V. I. Nikitenko, A. A. Polyanskii, R. L. Prozorov, I. V. Grekhov, L. A. Delimova, I. A. Liniichuk, A. V. Antonov, and M. Yu. Gusev, Superconductivity **5**(9), 1582 (1992).
[6] P. Brüll, D. Kirchgässner, and P. Leiderer Physica (Amsterdam) C **182**, 339 (1991).
[7] P. D. Grant, M. W. Denhoff, W. Xing, P. Brown, S. Govorkov, J. C. Irwin, B. Heinrich, H. Zhou, A. A. Fife, and A. R. Cragg, Physica (Amsterdam) C **229**, 289 (1994).
[8] W. Xing, B. Heinrich, H. Zhou, A. A. Fife, and A. R. Cragg, J. Appl. Phys. **76**, 4244 (1994).
[9] D. Reinel, W. Dietrich, A. Majhofer, and T. Wolf, Physica (Amsterdam) C **245**, 193 (1995).
[10] A. Gurevich and H. Küpfer, Phys. Rev. B **48**, 6477 (1993).
[11] C. P. Bean, Rev. Mod. Phys. **36**, 31 (1964); J. Appl. Phys. **41**, 2482 (1970).
[12] P. H. Kes, J. Aarts, J. van den Berg, C. J. van der Beek, and J. A. Mydosh, Supercond. Sci. Technol. **1**, 242 (1989).
[13] A. I. Larkin and Yu. N. Ovchinnikov, Zh. Eksp. Teor. Fiz. **61**, 1221 (1971) [Sov. Phys. JETP **34**, 651 (1972)].
[14] E. H. Brandt, Phys. Rev. Lett. **71**, 2821 (1993).
[15] E. H. Brandt, Phys. Rev. B **49**, 9024 (1994).
[16] E. H. Brandt, Phys. Rev. B **50**, 4034 (1994).
[17] M. V. Indenbom, Th. Schuster, H. Kuhn, H. Kronmüller, T. W. Li, and A. A. Menovsky, Phys. Rev. B **51**, 15 484 (1995).
[18] H. Theuss, A. Forkl, and H. Kronmüller, Physica (Amsterdam) C **190**, 345 (1992).
[19] P. N. Mikheenko and Yu. E. Kuzovlev, Physica C **204**, 229 (1993).
[20] J. Zhu, J. Mester, J. Lockhart, and J. Turneaure, Physica (Amsterdam) C **212**, 216 (1993).
[21] E. H. Brandt, M. Indenbom, and A. Forkl, Europhys. Lett. **22**, 735 (1993).
[22] E. H. Brandt and M. Indenbom, Phys. Rev. B **48**, 12 893 (1993); Physica B **194-196**, 1803 (1994); see also, W. T. Norris, J. Phys. D **3**, 489 (1970).
[23] E. Zeldov, J. R. Clem, M. McElfresh, and M. Darwin, Phys. Rev. B **49**, 9802 (1994).
[24] E. H. Brandt, Physica (Amsterdam) C **235-240**, 2939 (1994).
[25] Th. Schuster, M. V. Indenbom, H. Kuhn, E. H. Brandt, and M. Konczykowski, Phys. Rev. Lett. **73**, 1424 (1994); E. Zeldov, A. I. Larkin, V. B. Geshkenbein, M. Konczykowski, D. Majer, B. Khaykovich, V. M. Vinokur, and H. Shtrikman, *ibid.*, **73**, 1428 (1994).
[26] Th. Schuster, H. Kuhn, E. H. Brandt, M. Indenbom, M. R. Koblischka, and M. Konczykowski, Phys. Rev. B **50**, 16 684 (1994).
[27] Th. Schuster, M. V. Indenbom, M. R. Koblischka, H. Kuhn, and H. Kronmüller, Phys. Rev. B **49**, 3443 (1994).
[28] E. H. Brandt, Phys. Rev. Lett. **74**, 3025 (1995).
[29] E. H. Brandt (unpublished).
[30] J. Rhyner, Physica (Amsterdam) C **212**, 292 (1993).
[31] E. H. Brandt, Phys. Rev. B **46**, 8628 (1992).
[32] H. A. M. van den Berg, J. Appl. Phys. **60**, 1104 (1986).
[33] A. Forkl and H. Kronmüller, Physica (Amsterdam) C **228**, 1 (1994).
[34] Th. Schuster, H. Kuhn, and E. H. Brandt, Phys. Rev. B **51**, 697 (1995).
[35] E. H. Brandt, Rep. Progr. Phys. (to be published).
[36] L. A. Dorosinskii, M. V. Indenbom, V. I. Nikitenko, Yu. A. Ossip'yan, A. A. Polyanskii, and V. K. Vlasko-Vlasov, Physica (Amsterdam) C **203**, 149 (1992).
[37] Th. Schuster, M. R. Koblischka, N. Moser, B. Ludescher, and H. Kronmüller, Cryogenics **31**, 811 (1991).
[38] K.-H. Greubel, E. Gmelin, N. Moser, Ch. Mensing, and L.

Walz, Cryogenics **30**, Suppl., 457 (1990).
[39] M. R. Koblischka, N. Moser, B. Gegenheimer, and H. Kronmüller, Physica (Amsterdam) C **166**, 36 (1990).
[40] A. Erb, T. Traulsen, and G. Müller-Vogt, J. Cryst. Growth **137**, 487 (1994).
[41] H.-U. Habermeier, Eur. J. Solid State Inorg. Chem. **28**, 619 (1991).
[42] R. Szymczak, K. Piotrowski, H. Szymczak, and A. M. Balbashov, J. Magn. Magn. Mater. **92**, L19 (1990); Th. Schuster, M. R. Koblischka, N. Moser, and H. Kronmüller, Physica (Amsterdam) C **179**, 269 (1991); A. Forkl, H.-U. Habermeier, B. Leibold, T. Dragon, and H. Kronmüller, Physica (Amsterdam) C **180**, 155 (1991); Th. Schuster, M. R. Koblischka, B. Ludescher, and H. Kronmüller, J. Appl. Phys. **72**, 1478 (1992); Th. Schuster, M. R. Koblischka, H. Kuhn, B. Ludescher, M. Leghissa, M. Lippert, and H. Kronmüller, Physica (Amsterdam) C **196**, 373 (1992); V. K. Vlasko-Vlasov, M. V. Indenbom, and A. A. Polyanskii, in *The Real Structure of High-$T_c$ Superconductors*, edited by V. Sh. Shekhtman, Springer Series in Materials Science, Vol. 23 (Springer, Berlin, 1993), pp. 111–144.

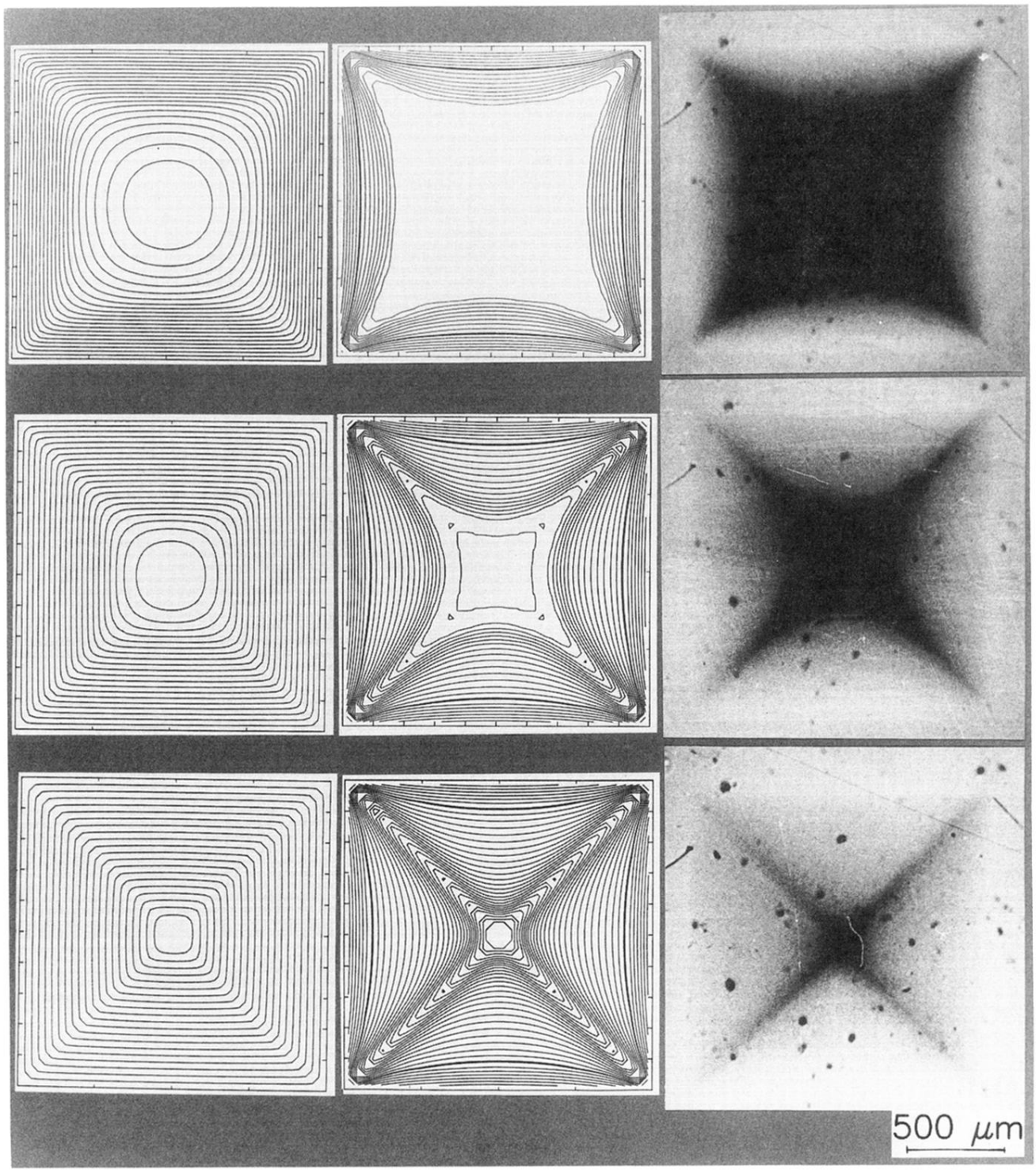


FIG. 3. Calculated current pattern (left column) and perpendicular field $H_z$ (middle column) distribution of a square sample for three different steps of flux penetration. Right column: Magneto-optically detected flux distributions in a square YBCO thin film at $T = 50$ K and $\mu_0 H_a = 54$ mT (top), 92 mT (middle), and 151 mT (bottom). The flux distributions were detected using a ferrimagnetic iron-garnet indicator. The black spots are defects in the indicator film. The film thickness is $d = 800$ nm. In the calculations the unit of the magnetic field (one fit parameter) is chosen such that best agreement is found with the observed flux distributions.

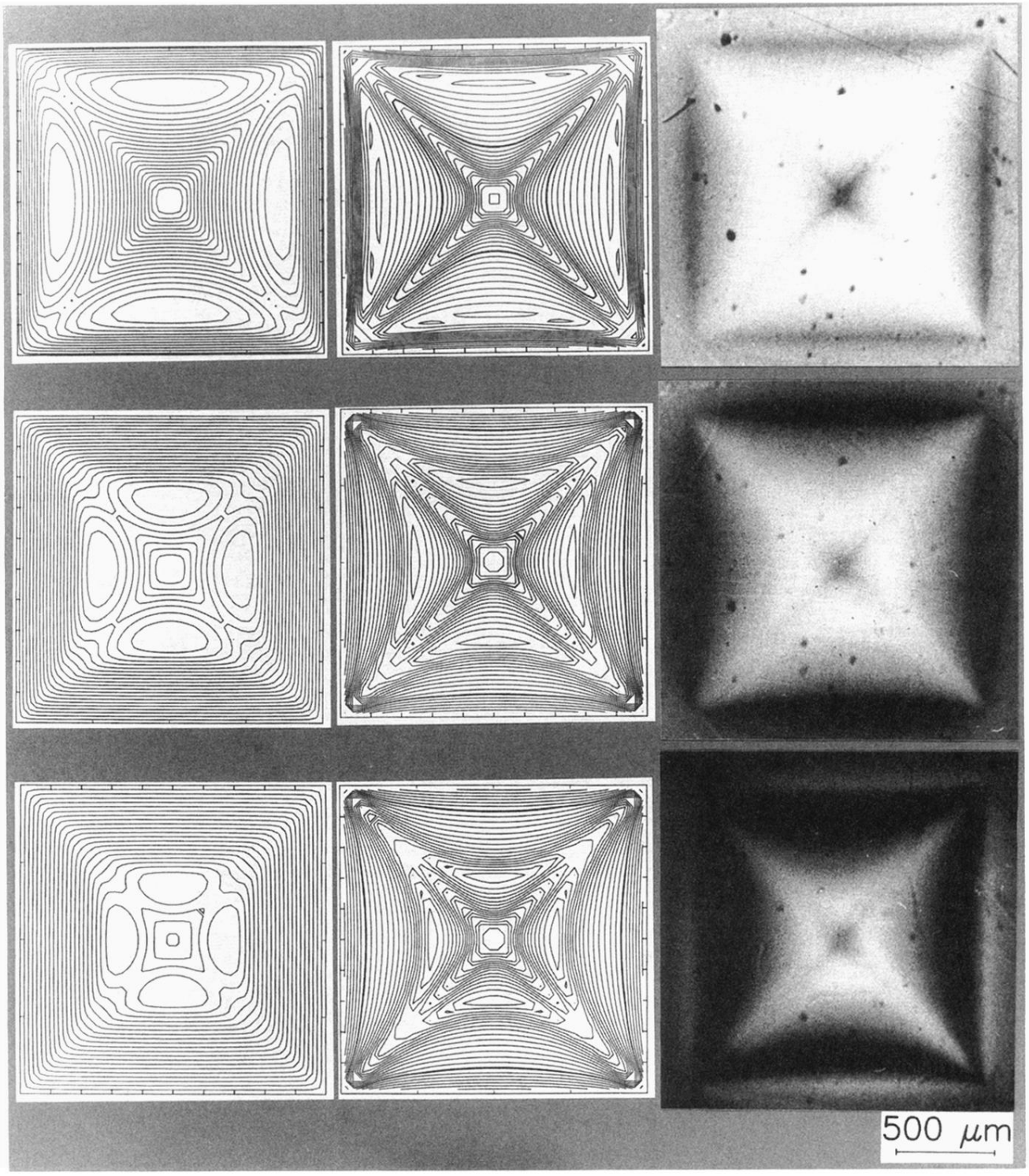


FIG. 4. As Fig. 3 but in decreasing magnetic field. Top: $\mu_0 H_a = 88$ mT, middle: 30 mT, bottom: 0 mT (remanent state).

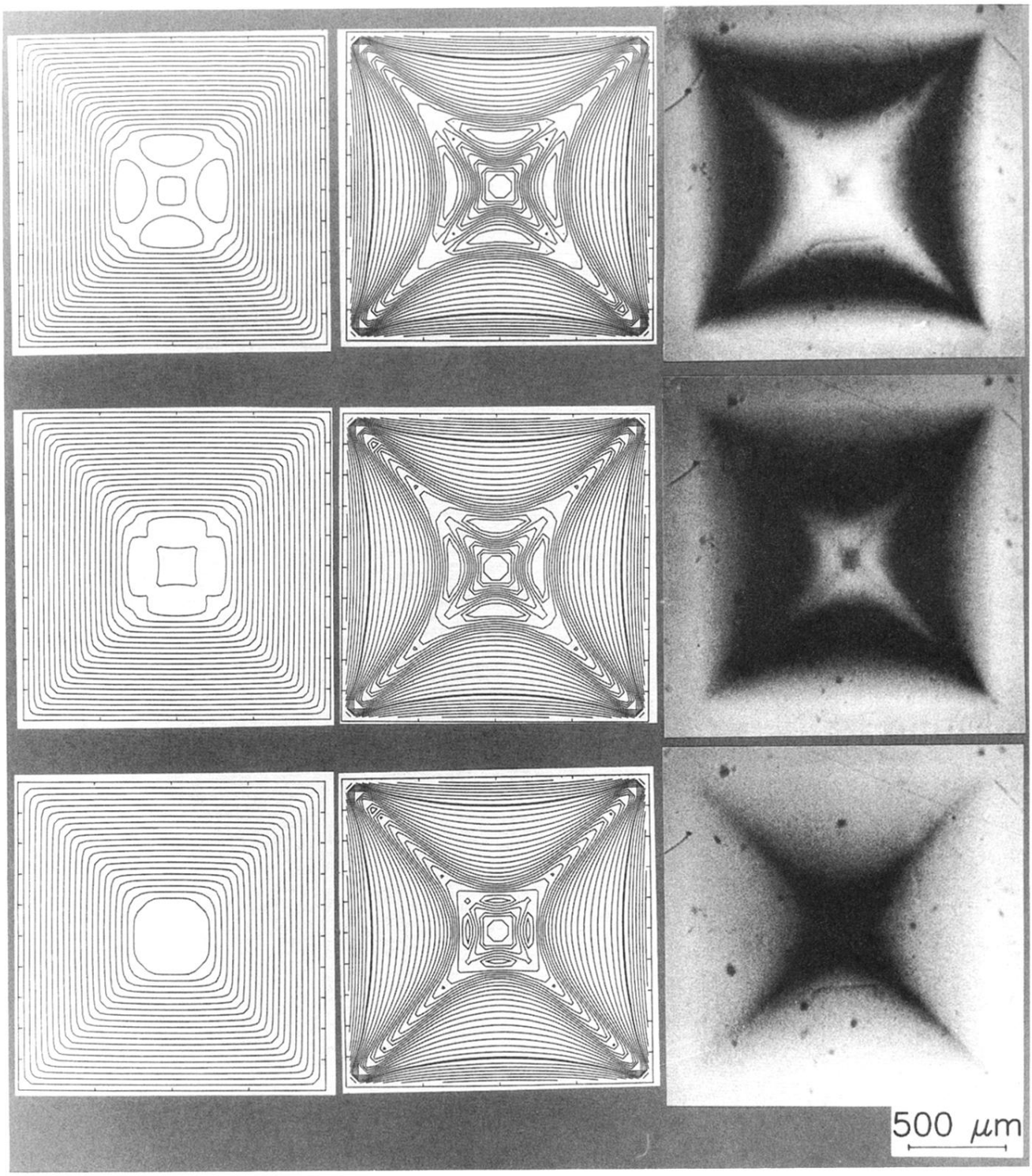


FIG. 5. As Fig. 3 but in reverse magnetic field. Top: $\mu_0 H_a = -24$ mT, middle: $-42$ mT, bottom: $-80$ mT.

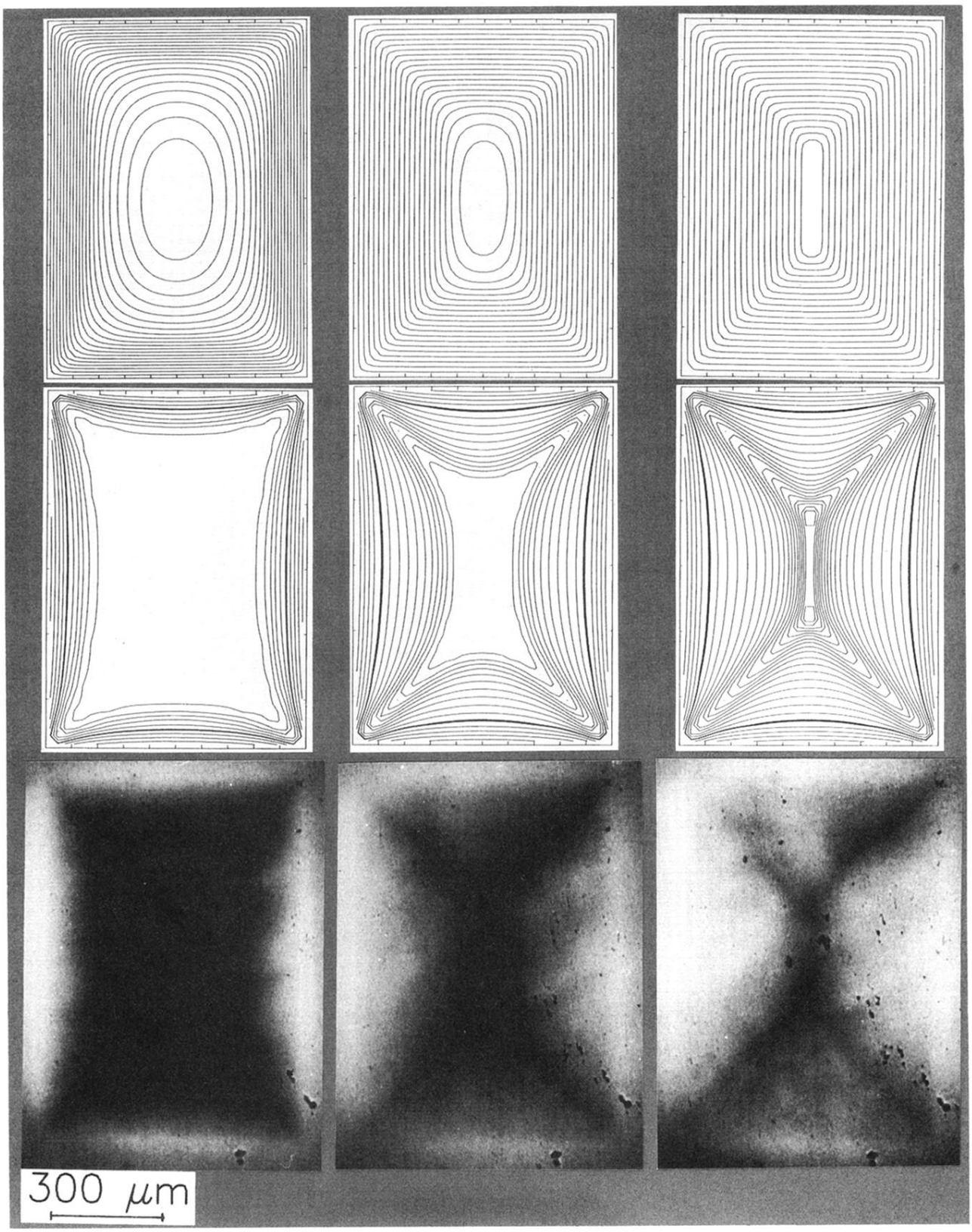


FIG. 6. Calculated current pattern (top) and field $H_z$ (middle row) in a rectangular sample for three different steps of flux penetration. Bottom: Magneto-optically detected flux distributions in a rectangular YBCO single crystal at $T = 30$ K and $\mu_0 H_a = 85$ mT (left), 171 mT (middle column), and 256 mT (right). The flux distributions were visualized using a ferrimagnetic iron-garnet indicator. The black spots are defects in the indicator film. The crystal thickness is $d = 20$ $\mu$m.

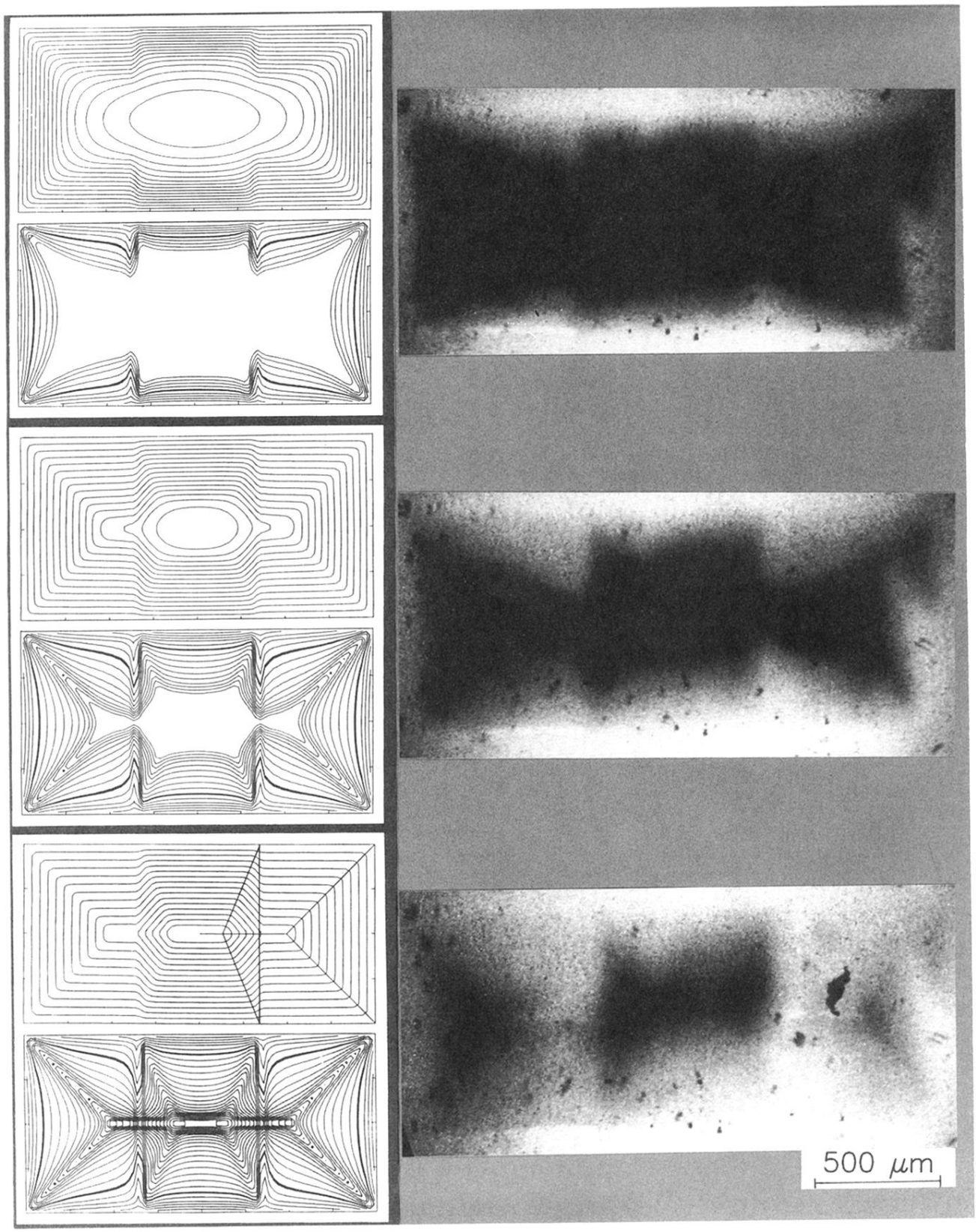


FIG. 7. Calculated current and flux patterns and magneto-optically determined flux distributions in a rectangular YBCO single crystal with inhomogeneous critical current distribution for three different magnetic fields of $\mu_0 H_a$ = 128, 213, and 299 mT (from top to bottom). The critical sheet current in the left and right part is about a factor 2/3 lower than the critical sheet current in the central region. For each magneto-optic image (right column) the calculated current distribution is located above the contour plot of the flux pattern (left column). Note the agreement between theory and experiment.